IEEE Robotics and Automation Letters (RA-L) paper, presented at ICRA 2024, Yokohama, Japan. Cite as RA-L paper.

Quadrolltor: A Reconfigurable Quadrotor with Controlled Rolling and Turning

Huaiyuan Jia, Runze Ding, Kaixu Dong, Songnan Bai, and Pakpong Chirarattananon, *Member, IEEE*

***Abstract*—This letter reports an aerial robot–Quadrolltor, with the ability to roll and turn. Existing bimodal quadrotors feature cylindrical rolling cages that are rotationally decoupled from the robot's main rigid body. In contrast, the proposed robot employs passively reconfigurable structures to enable the second mode of locomotion, tightly coupling the attitude of the robot to the rolling cage. The benefits are precise rolling and turning control as well as improved rolling efficiency. Experiments were conducted to comprehensively validate the hybrid locomotion. The robot leveraged the superior maneuverability in the rolling mode to take photos of the surroundings at different tilting and panning angles to construct a panoramic image. Besides, the results of the power measurements show a significant reduction in the cost of transport brought by at low speed, equating to a 15-fold extension in the operational range.**

***Index Terms*—Aerial Systems: Mechanics and Control, Mechanism Design, Wheeled Robots**

I. Introduction

ADVANCES in autonomous navigation [1]–[3] have led to the deployment of Micro Aerial Vehicles (MAVs) for a range of applications such as surveying [4], [5] and aerial transport [6]. However, the increasingly complex tasks and environments demand the robots to carry more payload and travel further. This is inevitably impeded by the high power requirement of flight. The issue aggravates with the relatively poor efficiency of rotorcraft [7], especially for smaller vehicles [8], [9]. The range and endurance rapidly become limiting factors, hindering these robots from wider uses.

Several avenues have been explored to raise the range and endurance of MAVs, depending on different operational needs. For tasks that demand a prolonged stay at elevation but involve minimal traveling (e.g., hovering), an alternative vehicle design with large rotating wings has been shown to halve the power consumption [9]. Similarly, hybrid aerial-surface locomotion or perching allows the robots to monitor the surroundings with lowered power consumption as they actively [10]–[12] or passively [13], [14] grasp [13], adhere to [10], [12], or rest/lean on [11], [14] nearby structures.

Alternatively, for missions entailing distant journeys, the bimodal aerial and terrestrial locomotion has emerged as a workaround solution to permit robots to fly over obstacles and traverse on ground to conserve energy. The ground phase is usually realized via either legged [15]–[18] or wheeled [19]–[25] locomotion. The walking or crawling motion benefits from the ability to deal with rough terrains, at the cost of sophisticated linkages [15], [17] or additional actuators [16], [18]. Despite this, crawling results in a 2.5-fold decrease in the cost of transport (COT) of the 30-gram hybrid quadrotor in [17], implying a substantial improvement in the operating range. Unsurprisingly, wheeled quadrotors have been shown to reduce the COT by up to a factor of 10 [21], [22], [26] when they roll at relatively low speeds.

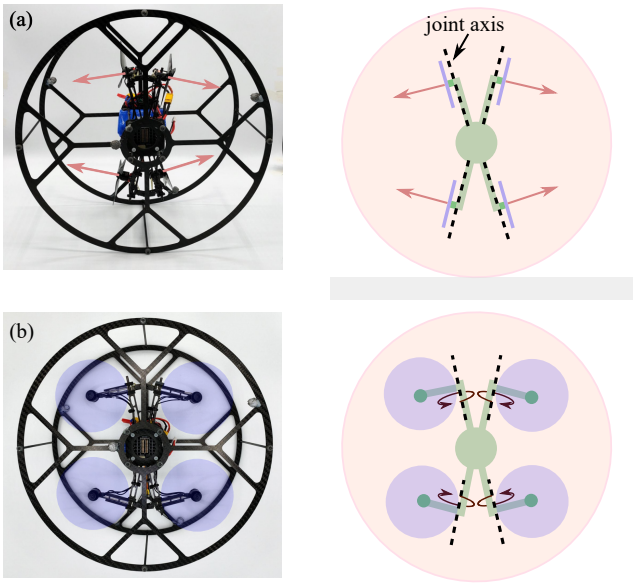

Fig. 1. Photos (left) and diagrams (right) of the Quadrolltor with passive joints in the (a) folded (rolling) and (b) unfolded (flying) states.

In this article, we propose to redesign a rotorcraft for the hybrid aerial and terrestrial locomotion, emphasizing rolling efficiency and terrestrial maneuverability. For existing hybrid rotorcraft [20]–[22], [26], the robots are attached to two large wheels on the sides through a low-friction axle. This way, the wheels are able to spin independently from the attitude of the robots. In order to roll, the robots pitch forward to create a forward thrust, similar to the flight strategy. In contrast, the proposed robot, depicted in Fig. 1 and the Supplementary Video, is rigidly fixed to two protective wheels and rolls by the rotation about its original yaw axis. To be able to efficiently generate the torque for rolling, we employ four passively reconfigurable joints. In the rolling mode, the

Manuscript received: March, 7, 2023; Accepted April, 22, 2023.

This paper was recommended for publication by Editor C. Gosselin upon evaluation of the Associate Editor and Reviewers' comments. This work was supported by the Research Grants Council of the Hong Kong Special Administrative Region of China (grant numbers CityU 11205419 and CityU 11215220). (*Huaiyuan Jia and Runze Ding are co-first authors.*) (*Corresponding author: Pakpong Chirarattananon.*)

The authors are with the Department of Biomedical Engineering, City University of Hong Kong, Hong Kong SAR, China (email: hhjia2-c@my.cityu.edu.hk; drunze2-c@my.cityu.edu.hk; pakpong.c@cityu.edu.hk).

Digital Object Identifier (DOI): see top of this page.

IEEE Robotics and Automation Letters (RA-L) paper, presented at ICRA 2024, Yokohama, Japan. Cite as RA-L paper.

IEEE Robotics and Automation Letters (RA-L) paper, presented at ICRA 2024, Yokohama, Japan. Cite as RA-L paper.

propelling axes are orthogonal to the rolling axis. As illustrated in Fig. 1a, the propeller directions permit the robot to readily produce positive or negative rolling torque, depending on which propeller is actuated. This results in precise controlled rolling and turning, as well as efficient low-speed rolling.

The key components that enable the robot to roll in the mentioned configuration without the need for extra actuators are the passive joints. The revolute joints, which default in the folded state owing to the pre-stretched elastic components, unfold and the robot transforms to the flight configuration when the generated thrusts are sufficiently large. The concept of passive morphological adaptation has been previously employed in MAVs for enhancing the maneuverability [27], safe interactions with the environments [28], [29], and enabling aerial-aquatic locomotion [30]. In this work, it is used to realize aerial-terrestrial locomotion.

The Quadrolltor shown in Fig. 1 is further developed from our previous work [24], which featured only two passive joints. In the rolling mode, the two rotors can only generate positive torque for rolling forward. This results in very limited rolling control. Compared to [24] and other wheeled quadrotors [20]–[22], [24], the configuration in this work allows the robot to generate both positive and negative rolling torque, as well as turning torque. The robot can precisely realize rolling and turning angular setpoints in the rolling mode. It becomes possible for the robot to track a complex terrestrial trajectory or take still photos of the surroundings with an onboard camera at different panning and tilting angles in the rolling mode. Furthermore, compared to the conventional hybrid robots [20]–[22], [26], the robot in [24] and this work can negotiate small openings with the gap-to-drone ratio [31] of ≈ 0.5, rivaling the state of the art [31], thanks to the narrow profile in the rolling mode. This is advantageous for operations in cluttered environments.

To sum up, this article proposes a rotorcraft with the ability to roll with precision and efficiency. The actuation of the robot in both locomotion modes is achieved only by the four propellers, based on the use of passive joints to re-orient the thrust vectors according to the commands. The design lowers the power consumption in rolling, extending the feasible mission range.

This paper is organized as follows. The design of the robot is discussed in the next section. The analysis suggests the robot is potentially more efficient in rolling than existing hybrid quadrotors. Section III describes the dynamics of the robot in the terrestrial modes, including the strategy for controlled rolling and turning. In Section IV, we fabricated the prototype and conducted experiments to demonstrate the rolling capability of the robot and measure the power consumption. Lastly, a conclusion is provided in Section V.

II. Reconfigurable Design for Rolling Efficiency

Hybrid terrestrial locomotion of quadrotors via rolling has been previously demonstrated in [20], [21], [26] with the design of a quadrotor hinged at the center of a cylindrical cage as shown in Fig. 2a. Recently, we proposed an alternative design that leverages two reconfigurable arms for the robot to roll with the benefit of having a narrow body in the rolling mode [24], allowing the robot to negotiate passages as narrow as 10 cm. In this section, we first show that the design based on the robot in [24], but with four passive revolute joints (depicted by Fig. 2b), can improve the rolling efficiency and maneuverability compared with the conventional design captured by Fig. 2a. Then, we outline how the proposed design can be realized or how the different configurations in the aerial and terrestrial modes can be achieved via passive joints.

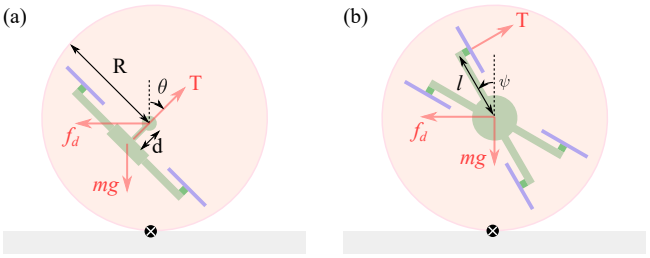

Fig. 2. Equilibrium conditions for rolling at constant speed. Ground normal forces are omitted and ground friction is absent when the speed is constant. (a) The design of previous rolling quadrotors, in which the robot's attitude is decoupled from the rolling cage. (b) The proposed design. The same angle ψ characterizes both the rolling angle and the orientation of the robot.

A. Design Comparison

Here, we provide a high-level analysis to obtain the minimal net thrust T for the robots in Fig. 2 need to generate to sustain a constant rolling speed v. The design with lower T is then presumed to be more efficient in rolling.

1) Conventional design: For rolling quadrotors in [20], [21], [26], their design is abstracted in Fig. 2a. The robot body is offset from the main axis of a lightweight cylindrical frame of radius R by some distance d. With the frictionless revolute joint [21], the attitude of the robot is decoupled from the rolling motion of the cage. When rolling, the robot may pitch forward by an angle θ. When rolling forward at speed v, the robot is subject to aerodynamic drag f_d in the direction opposite to the translational motion, assumed to be acting at the center of the cage. The drag is presumed to be proportional to the translational speed v as $f_d = bv$.

To obtain the equilibrium condition for rolling without slipping, we inspect the rotational dynamics. Since the ground contact point is instantaneously at rest, it is taken as a reference for deriving the equation for the balance of moment (using the contact point as a reference eliminates the need to explicitly consider the normal force and friction). With the rotational axis, the torque produced by the robot is not propagated to the rolling cage. Only the force (net thrust T and weight mg) is transferred to the rotating wheel via the shaft. As a result, the balanced moment condition for the robot in Fig. 2a is $TR\sin\theta - bvR = 0$, independent of mg and d. The optimal configuration for maximizing the rolling speed v for a given net thrust T is with $\theta = 90°$. That is the robot pitches fully forward. The equation reduces to

$$T = bv, \tag{1}$$

which states that the thrust T and the drag $f_d = bv$ cancel. In practice, $\theta < 90°$ is usually preferred to simplify the control

IEEE Robotics and Automation Letters (RA-L) paper, presented at ICRA 2024, Yokohama, Japan. Cite as RA-L paper.

IEEE Robotics and Automation Letters (RA-L) paper, presented at ICRA 2024, Yokohama, Japan. Cite as RA-L paper.

problem [21], such configuration would render the robot less efficient in rolling. Moreover, as θ approaches 90°, the robot cannot readily decelerate or reverse the rolling direction.

2) Proposed design: The robot in this work takes a shape dissimilar to a regular quadrotor when it is in the rolling mode. In this design (Fig. 2b), the robot's attitude is fully coupled with the outer frame. We define ψ to describe the instantaneous orientation of the robot and l to be the distance from the center to each propeller. While rolling, only one upper propeller is actuated with the generated thrust T. The robot is subject to similar drag $f_d = bv$. The balance of moment condition, taken about the ground contact point is

$$T(R\cos\psi + l) - bvR = 0, \tag{2}$$

which is dependent on ψ. To reduce the magnitude of T required, one may consider a ψ-dependent T command such that T is increased when $\cos\psi$ is positive and decreased when $\cos\psi$ is negative. For instance, when $T(\psi) = T_0(1+\cos\psi)$, $T(\psi)$ becomes T_0 on average and (2) averages to

$$T_0 = bv\left(1 - (2l - R)/(2l + R)\right). \tag{3}$$

Comparing (1) with (3), it can be seen that the proposed design requires lower thrust to overcome the same amount of drag force as long as $l > R/2$. Or, in an ideal case, if T is chosen as an impulse: $T(\psi) = T_0\delta(\psi)$, we find

$$T_0 = bv\left(1 - l/(l + R)\right). \tag{4}$$

That is, $T_0 < bv$ as long as $l > 0$. The proposed design is deemed more effective. This is despite the fact that we have neglected the joint friction and the the need to actively control the attitude in the conventional design. As per momentum theory, power relates to thrust according to $P \propto T\sqrt{T}$ [7], [9]. This means the proposed design is anticipated to be more efficient in rolling than the previous robots. Besides, if some propellers are arranged oppositely as illustrated in Fig. 2b, the robot is able to quickly reverse the rolling motion. This is unlike the design in Fig 2a, in which the attitude change must be accomplished to alter the rolling direction.

B. Reconfigurable Airframe

The robot configuration for rolling and turning differs from a regular quadrotor design. Hence, a reconfigurable airframe with four passive revolute joints is devised to allow the robot to transform between various configurations to achieve the hybrid locomotion. The proposed design, shown in Fig. 1 and the Supplementary Video, slightly deviates from our previous prototype [24], in which only two passive joints are present.

The reconfigurable airframe comprises four passive joints (Fig. 1), accommodating four propelling arms. Incorporating elastic elements, these joints default in the 90° folded state. When a propeller spins fast enough to generate sufficient torque to overcome the restoring torque, the joint unfolds. The flight mode is achieved when all joints are fully unfolded. The propeller axes are then aligned with principal axis of the cylindrical cage and the robot behaves as a regular quadrotor.

The configuration of the rolling mode is schematically shown in Fig. 2b. In the folded state, the propeller axes are perpendicular to the rolling axis. When lightly actuated, the joint remains folded and the thrust induces the rolling torque. With the design in Fig. 2b, two propellers generate positive rolling torque and the other two produce negative rolling torque. Hence, the robot is able to roll forward and backward, or accelerate and decelerate, depending on which pair of the propellers are activated.

To create a turn in the terrestrial mode after the robot comes to a halt, one propeller is actuated with a sufficiently high command so that the joint unfolds and the rotor axis becomes parallel to the rolling axis. The distance between the rotor axis and the rolling axis represents the moment arm of the turning torque, which is amplified when this lies horizontally.

C. Passively Reconfigurable Joints

Without additional actuators, the passive revolute joints are the key feature that equips the robot with the terrestrial locomotion. As introduced above, each spring-loaded joint has one rotational degree of freedom. The joint design is highly similar to those in our previous work [24].

Fig. 3a highlights the mechanical design. The propelling arm is attached to the central airframe (mechanical ground) via a revolute joint. A pre-stretched elastic component connects the two links. Joint stoppers are incorporated to restrict the motion to 90°. By default, the contracting force keeps the joint in the folded state. When the thrust prevails the restoring force, the joint unfolds. By strategically selecting suitable parameters (such as the stiffness and natural length of the elastic component), the joints meet the requirements of both modes of locomotion as detailed in [24].

III. Modeling and Control for Hybrid Locomotion

In this section, we begin with the introduction of the robot's physical parameters and the relevant coordinate frames. Then, we present the modeling and control for hybrid locomotion, with the emphasis on controlled rolling and turning.

A. Configurations and Coordinate Frames

Fig. 3b and c depicts a robot standing on the ground. For an illustration purpose, three of the revolute joints (joints 1, 2, and 3) are folded and the 4^{th} joint is shown unfolded. The body frame $\{\boldsymbol{x}_B, \boldsymbol{y}_B, \boldsymbol{z}_B\}$ is located at the center of mass (CM). To describe the rolling and turning motion, we define the ground contact frame $\{\boldsymbol{x}_C, \boldsymbol{y}_C, \boldsymbol{z}_C\}$. By definitions, $\boldsymbol{z}_C$ and $\boldsymbol{z}_B$ align, while $\boldsymbol{y}_C$ points vertically up.

We let an index $i \in \{1, 2, 3, 4\}$ represent the i^{th} propeller and $\boldsymbol{n}_i$ be unit vectors indicating the axes of the folding joints parallel to the inner propeller arms, defined in the body frame (pointing radially inward or outward, indicating the unfolding direction). As seen in Fig. 3b and c, the inner propeller arms of length l_n are offset from the center of mass by the distance l_h along $\boldsymbol{z}_B$. The position of the i^{th} propeller with respect to the body frame when folded is denoted by $\boldsymbol{l}_{i,f} = l_h\boldsymbol{e}_3 \pm l_n\boldsymbol{n}_i - l_o\boldsymbol{e}_3$ with l_o being the length of the folding link. When unfolded (e.g. propeller 4 in Fig. 3b), the location of the i^{th} propeller becomes $\boldsymbol{l}_{i,u} = l_h\boldsymbol{e}_3 \pm l_n\boldsymbol{n}_i + l_o\boldsymbol{e}_3 \times \boldsymbol{n}_i$.

IEEE Robotics and Automation Letters (RA-L) paper, presented at ICRA 2024, Yokohama, Japan. Cite as RA-L paper.

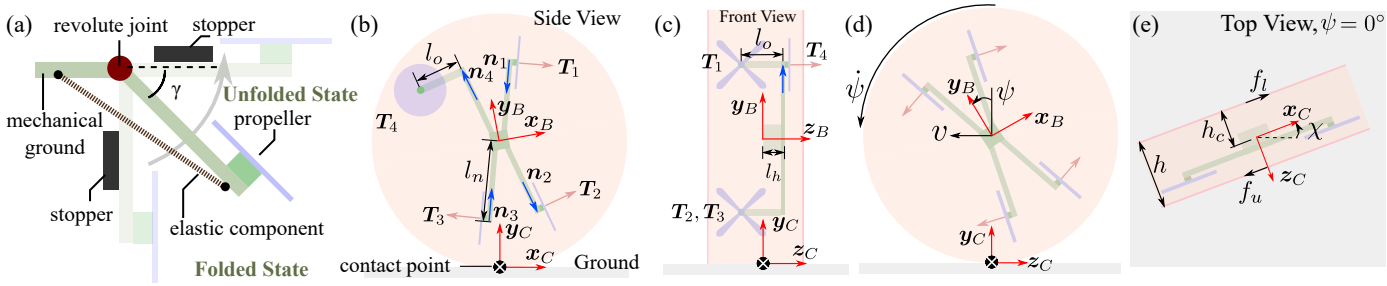

Fig. 3. Diagrams of the passive joint and the robot in the terrestrial mode. (a) The joint angle γ is $90°$ when folded and $0°$ when unfolded. (b) Definitions of vectors and arm lengths from the side. (c) Definitions of vectors and arm lengths from the front. (d) Rolling configuration. (e) Turning dynamics.

B. Aerial Locomotion

The realization of flight is relatively straightforward provided that the robot starts with the upright orientation (the axis $\boldsymbol{z}_B$ directs upward). Because of the spring-loaded joints, the propellers are in the folded position when unactuated. However, when the thrust of each propeller exceeds $0.15mg$ (this number is chosen and designed using the method outlined in Section II-C and [24]), it unfolds and the robot takes the form of a regular quadrotor. In the previous work [24], we verified with a similar but not identical robot that a conventional flight controller based on the linearized flight dynamics was effective without the need for any modifications. In this work, a similar approach is employed for flight stabilization and trajectory following in the experiments.

C. Dynamics and Control for Wheeled Locomotion

In this work, rolling and turning are considered separately. This reduces the motion in each case to one degree of freedom, simplifying the control problems without significantly affecting the capability of the robot.

1) Rolling dynamics and control: Considering rolling without slipping, the rolling motion can be entirely described by the yaw angle ψ (defined as the angle between $\boldsymbol{y}_B$ and $\boldsymbol{y}_C$ measured about $\boldsymbol{z}_C$) as shown in Fig. 3d. The rotational dynamics of the robot is derived with respect to the origin of the ground contact frame, which is instantaneously at rest, as

$$(J_\psi + mR^2)\ddot{\psi} = \tau_\psi, \tag{5}$$

where J_ψ is the yaw inertia of the robot, and τ_ψ is total torque acting on the robot with respect to $\boldsymbol{z}_C$. To regulate the rolling motion, a PD controller is proposed to compute the desired torque $\tau_{\psi,d}$. We let ψ_d denote the desired rolling angle such that the angular error becomes $\psi - \psi_d$. The PD control law is

$$\tau_{\psi,d} = (J_\psi + mR^2)\ddot{\psi}_d - k_{\psi,d}(\dot{\psi} - \dot{\psi}_d) - k_{\psi,p}(\psi - \psi_d), \tag{6}$$

where $k_{\psi,\cdot}$'s are positive gains. The closed-loop dynamics guarantee $\psi \to \psi_d$ if $\tau_\psi \to \tau_{\psi,d}$. Notice that the parameters in (6) can be adjusted for two different objectives. When the proportional gain $k_{\psi,p}$ is zero, the controller only regulates the angular rate rolling velocity. This is suitable for distant rolling. On the other hand, if $\dot{\psi}_d$ is chosen as zero, (6) directly controls the angle ψ. This is equivalent to controlling the robot's position. Lastly, to ensure $\tau_\psi \to \tau_{\psi,d}$, the implemented torque generation method is described below in Section III-C3.

2) Turning dynamics and control: To alter the travel direction on the ground, a strategy for turning is devised. A turning maneuver is only executed when the robot is not rolling (this can be accomplished by controlling the rolling angle ψ to be constant). To generate the turning torque (about the axis $\boldsymbol{y}_C$), one propeller is actuated at a relatively large command so the joint unfolds. A counter torque can be produced in a similar fashion by another propeller if needed.

The dynamics associated with turning is captured by Fig. 3e. The rolling angle χ is defined as the rotation about the axis $\boldsymbol{y}_C$, which passes vertically through the CM, with respect to some reference. We let τ_χ be the actuated torque in the direction of $\boldsymbol{y}_C$ (how this is generated is detailed in Section III-C3). The turning motion results in the relative displacement between the contact points of the rims of the cage and the ground in the direction parallel to $\boldsymbol{x}_C$. This results in the opposing friction forces f_u and f_l. As a consequence, the equation of motion is

$$J_\chi \ddot{\chi} = \tau_\chi - f_u(h - h_c) - f_l h_c, \tag{7}$$

where J_χ is the moment of inertial of the robot computed with respect to the axis $\boldsymbol{y}_C$. In practice, this can be approximated as the average between the roll and pitch inertias. Herein, h denotes the width of the robot in this configuration and h_c is the distance from the base face to the CM. By design, the CM is located near the center of geometry, rendering $h - h_c \approx h_c \approx h/2$. This reduces (7) to $J_\chi \ddot{\chi} = \tau_\chi - (f_u + f_l)h/2$. Both f_u and f_l are related to the friction coefficient μ and the ground normal forces. Since the sum of the normal forces equals to the weight of the robot mg, the equation becomes

$$J_\chi \ddot{\chi} = \tau_\chi - \mu mgh/2. \tag{8}$$

As a consequence, the turning angle χ can be controlled to the desired angle χ_d using the following linear control law

$$\begin{aligned}\tau_{\chi,d} =& \mu mgh/2 + J_\chi \ddot{\theta}_d - k_{d,\chi}(\dot{\chi} - \dot{\chi}_d) \\ & - k_{\chi,p}(\chi - \chi_d) - k_{\chi,i}\textstyle\int (\chi - \chi_d)\,\mathrm{d}t,\end{aligned} \tag{9}$$

where $k_{\chi,\cdot}$'s are positive control gains. Notice that unlike the rolling controller described by (6), the integral term is included. The compensation provided by the integral term can deal with model uncertainties and drastically improve the turning performance. For example, in the case that the propeller thrust, which is aligned with $\boldsymbol{z}_B$, induces some friction component in the direction of $\boldsymbol{z}_B$ or $(\boldsymbol{z}_C)$, the sum of f_u and f_l component in the direction parallel to $\boldsymbol{x}_C$ may

IEEE Robotics and Automation Letters (RA-L) paper, presented at ICRA 2024, Yokohama, Japan. Cite as RA-L paper.

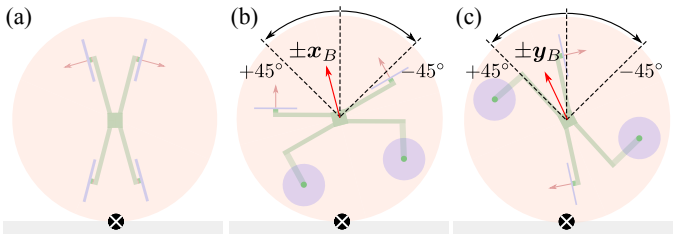

Fig. 4. Rolling and turning torque generation. (a) The upper pair of propellers are used for rolling. (b) When $\boldsymbol{x}_B$ is within 45° of the vertical, two lower propellers are responsible for producing the turning torque. (c) When $\boldsymbol{y}_B$ is within 45° of the vertical, two opposite propellers are responsible for producing the turning torque.

be smaller than μmg as assumed by (8). Furthermore, it is difficult to precisely estimate the friction coefficient μ between the robot and the ground surface. These factors render the term $\mu mgh/2$ in (9) highly imprecise. The use of the integral term can efficiently handle the modeling uncertainties and ensure that $\chi \to \chi_d$ provided that τ_χ approaches $\tau_{\chi,d}$.

3) Rolling and turning torque generation: To evaluate the maps from T_i's to τ_ψ and τ_χ, we neglect the drag torque of the propellers as the thrust components dominate. In the rolling mode, a pair of folded propellers further away from the ground contact (pointing approximately horizontally) is used to generate positive and negative τ_ψ. For instance, for $-90^\circ \leq \psi < 90^\circ$ (see Figs. 3d and 4a), T_1 and T_4 are chosen. In the ground contact frame, $R\boldsymbol{e}_2 + \boldsymbol{R}_z(\psi)\boldsymbol{l}_{i,f}$ is the position of the i^{th} propeller and $\boldsymbol{R}_z(\psi)(\boldsymbol{e}_3 \times \boldsymbol{n}_i)$ is the force direction provided that $\boldsymbol{R}_z(\psi)$ is the rotation matrix. Therefore,

$$\tau_\psi = \textstyle\sum_{i=1,4} \boldsymbol{e}_3^T(R\boldsymbol{e}_2 + \boldsymbol{R}_z(\psi)\boldsymbol{l}_{i,f}) \times \boldsymbol{R}_z(\psi)(\boldsymbol{e}_3 \times \boldsymbol{n}_i), T_i \tag{10}$$

and the sum changes to $i = 2, 3$ for $90^\circ \leq \psi < 270^\circ$. In comparison, the previous robot with only two folded arms [24] cannot generate negative rolling torque. The new configuration improves the efficiency and rolling control as outlined earlier.

In the turning mode, two propellers are reserved for producing the rolling torque τ_ψ (to keep the rolling angle ψ constant) and the other two propellers are assigned for creating the turning torque τ_χ. The combination depends on the instantaneous ψ angle. To make sure it is always possible to generate both positive and negative turning torque, two bottom propellers are used for turning when the axis $\boldsymbol{x}_B$ is within 45° of the vertical (Fig. 4b), leaving the other two for controlling ψ. On the other hand, when the axis $\boldsymbol{y}_B$ is within 45° of the vertical (Fig. 4c), two opposite propellers that are further apart are used for turning and the other pair is used for stabilizing ψ. The generated rolling torque is the same as (10), but the sum is over different propellers. To compute the mapping for the turning torque, we determine the torque with respect to the body frame as $\sum_i \boldsymbol{l}_{i,u} \times \boldsymbol{e}_3 T_i$. The turning torque is this torque projected on to the $\boldsymbol{y}_C$ axis:

$$\tau_\chi = \textstyle\sum_i \boldsymbol{e}_2^T \boldsymbol{R}_z(\psi)(\boldsymbol{l}_{i,u} \times \boldsymbol{e}_3 T_i), \tag{11}$$

where the sum is for the corresponding pair of propellers. Lastly, the thrust commands can be evaluated based on $\tau_{\psi,d}$ and $\tau_{\chi,d}$ by inverting (10) and (11).

D. Transitions Between Aerial and Terrestrial Modes

The methods to switch between the two operating modes were proposed for the robot with two passive joints [24]. The techniques are applicable to the Quadrolltor. In here, we briefly outline the procedures for completeness.

1) Transitions from flight to terrestrial mode: The switch from flying to rolling is simple in comparison. After landing, a single contact point on the ground is chosen as a pivot. A combination of propelling commands is used to generate torque about a horizontal axis that passes through the pivot. To do so, the commands must be sufficiently large to unfold the propelling arms. Propellers located further away from the pivot are preferred to amplify the moment arms.

2) Transitions from the terrestrial to flight mode: The transition from the rolling state to flight is accomplished by a dynamic maneuver. This is because in the rolling state, the torque produced by folded propellers can only accelerate or decelerate the rolling motion. Meanwhile, the torque produced by an unfolded propelling arm would induce the robot to turn upside down instead. The solution we showed in [24] makes use of the nonlinear property of rotations. By timely commanding the robot to suddenly turn while rolling, the addition of two angular velocity vectors flips the robot in the desired direction. The robot then completes the maneuver with its $\boldsymbol{z}_B$ axis orienting upward.

IV. Experimental Validation

To validate the effectiveness of proposed hybrid aerial terrestrial quadrotor, several experiments were carried out as summarised in the Supplementary Video.

A. Prototype Fabrication

The outer airframe was constructed from 3-mm-thick carbon fiber sheets and carbon fiber rods (3 mm in diameter). The radius of the outer airframe is $R = 160$ mm; and the robot height is $h = 150$ mm, resulting in the gap-to-drone ratio [31] of < 0.5. When lying flat, the distance from the ground to the CoM is $h_c = 80$ mm. The offset from the inner airframe to the CoM is $l_h = 35$ mm. We employed four brushless motors (EMAX ECO 1106 4500KV) with 3.5-inch 3-blade propellers. The motors were mounted symmetrically on the passive joints with the length of the inner arm $l_n = 77$ mm. The length of the folding arm is $l_o = 48.5$ mm. Rubber bands with the resting length $l_0 = 30$ mm and linear stiffness $k_e = 214$ N/m were adopted as elastic components for the passive joints.

A flight control board (Bitcraze, Crazyflie Bolt) and a 4-in-1 electronic speed controller (HAKRC) were incorporated. The robot is powered by a 3000-mAh 2S battery. For measuring the power consumption, we employed a Raspberry Pi Zero 2 W with a separate ADC (ADS1115) to log the voltage (Risym, 1:5 divider ratio) and current (Risym, ACS712ELC-20A) of the battery. To enable a reliable outdoor flight, an onboard positioning device (Bitcraze, Flowdeck v2) was employed. The board contains time-of-flight and optical flow sensors, allowing the robot to reliably regulate its altitude and translational speed without visual odemetry. The total mass of the Quadrolltor, shown in Fig. 1, is $m = 350$ g.

IEEE Robotics and Automation Letters (RA-L) paper, presented at ICRA 2024, Yokohama, Japan. Cite as RA-L paper.

B. Experiment Setup

Indoor experiments were conducted with the motion capture (MOCAP) system (OptiTrack Prime 13W) for providing position feedback and ground-truth measurements. The attitude feedback was provided by an onboard inertial sensor through a complimentary filter. A ground station computer running Python scripts communicated with the Crazyflie Bolt through radio for sending commands and data logging.

C. Demonstration of Flights and Transitioning Maneuvers

1) Aerial locomotion: We first verified flight ability by instructing the robot to fly through several waypoints. The flight was conducted in the arena with the MOCAP system used for the position feedback. With a standard cascaded flight controller described in [24], the robot flew over 5.81 m in 25 s at a constant altitude. The realized and reference trajectories are plotted in Fig. 5a. The root mean square error (RMSE) of the position is 4.1 cm. The outcome confirms that the flight performance is not visibly affected by the use of passive joints as the airframe remained sufficiently rigid at relatively large propeller commands as designed.

2) Transition from flight mode to rolling mode: Next, we show that the transitioning method developed in [24] for the previous generation smaller robot with two passive joints remains effective for the robot in this work. To do so, the transition angle is defined as the angle between the Z_B axis and the vector normal to the ground. By controlling the thrust of suitable propellers, the robot used the edge of the bottom wheel in contact with the ground as a non-slip hinge to transition the transition angle from 0° to 90°, ending in the rolling configuration as depicted in Fig. 6a. The maneuver was completed within 2.7 s as plotted in Fig. 5b.

3) Transition from rolling mode to flight mode: To make the transition back, the robot was controlled to roll at a constant rate. While rolling, one free propeller was actuated and unfolded. This immediately added the vertical component (as seen in the inertial frame) to the existing horizontal angular velocity vector. The resultant angular velocity made the robot fell into the flight mode (Fig. 6b). The transition angle dropped from 90° to 0° in about 2 s as shown in Fig. 5b.

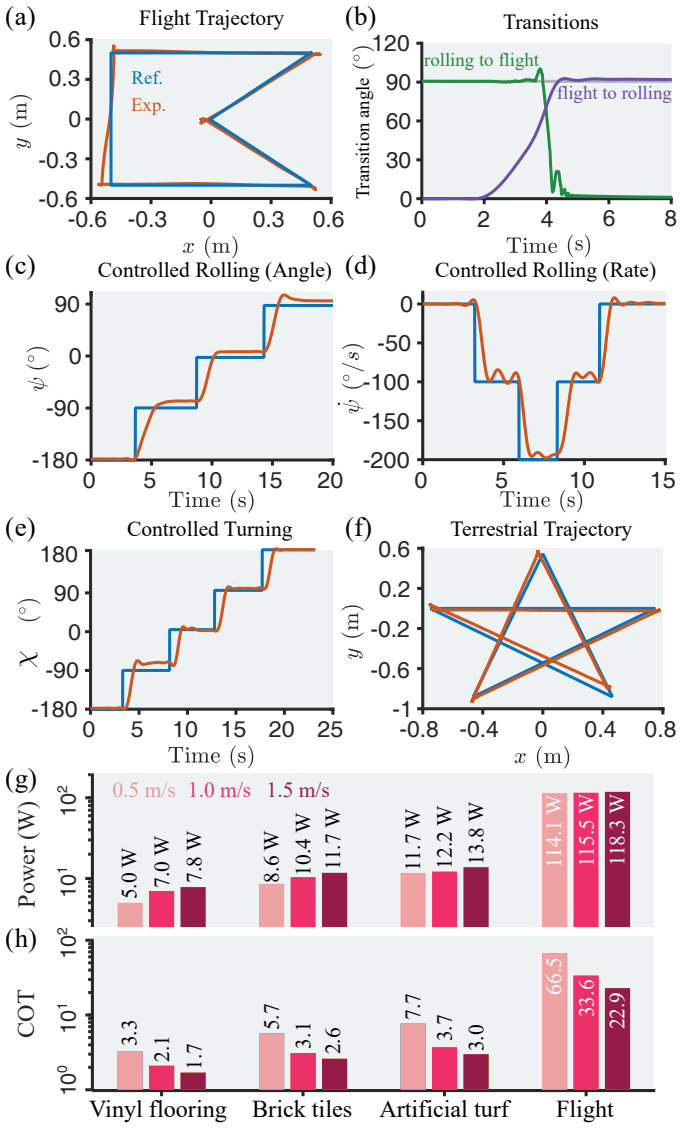

Fig. 5. Experimental results. (a) Flight trajectory. (b) Transitions between the flight mode and rolling mode. (c) Results of controlled rolling with step angular setpoints. (d) Results of controlled rolling with rate setpoints. (e) Results of controlled turning. (f) Realization of Pentagram trajectory. (g) Power consumption of the robot at three traveling speeds. (h) Cost of transport.

D. Precise Controlled Rolling and Turning

We validate the robot's terrestrial locomotion by extensively examining its rolling and turning maneuvers using the controllers detailed in Section III-C1. In these tests, only the onboard feedback was required.

1) Rolling and turning: To begin, the robot was commanded to track five reference yaw angles in 90° steps, completing one cycle of rotation as seen in Fig. 6c. With the step changes, the robot took approximately 1.6 s to deal with each sudden change in the reference as shown in Fig. 5c. Despite the non-negligible response time, the RMSE in rolling angle over the 20-s period is 32.3° with small averaged steady error (6.0°). The result illustrates the robot's ability to accelerate and decelerate in the rolling mode despite the absence of additional actuators. In comparison, the controlled rolling was infeasible in our previous prototype in [24]. The precise angular control was also difficult to achieve and not demonstrated by the hybrid quadrotors in [21], [26].

Fig. 5d displays the result when robot was commanded to rolling at specified rates. The setpoint rates were -100 and -200 deg/s (corresponding to v = 0.56 m/s). The robot took about 1 s to react to the step changes. The RMSE over the 15 s trajectory is 25.4 deg/s, with the averaged steady error of 6.8 deg/s. The effectiveness of the simple controller is a consequence of the robot's rolling configuration.

To demonstrate controlled turns based on the strategy in Section III-C2, we first commanded the robot to maintain a constant yaw angle of 0°. Then, the turns were made by adjusting the setpoints with the increment of 90° from -180° to 180° as captured by Figs. 5e and 6d. Again, the robot needed approximately 2 s to complete each turn. This results

IEEE Robotics and Automation Letters (RA-L) paper, presented at ICRA 2024, Yokohama, Japan. Cite as RA-L paper.

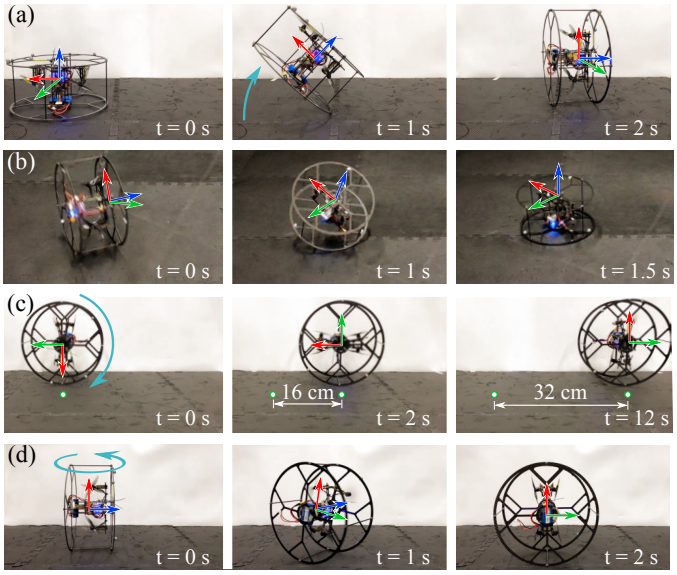

Fig. 6. Photos of the experiments. (a) The transition from flight mode to rolling. (b) The transition from rolling to the flight configuration. (c) Controlled rolling. The robot rolled as a result of the change in the angular setpoint with 90° steps. (d) A 90-degree turn.

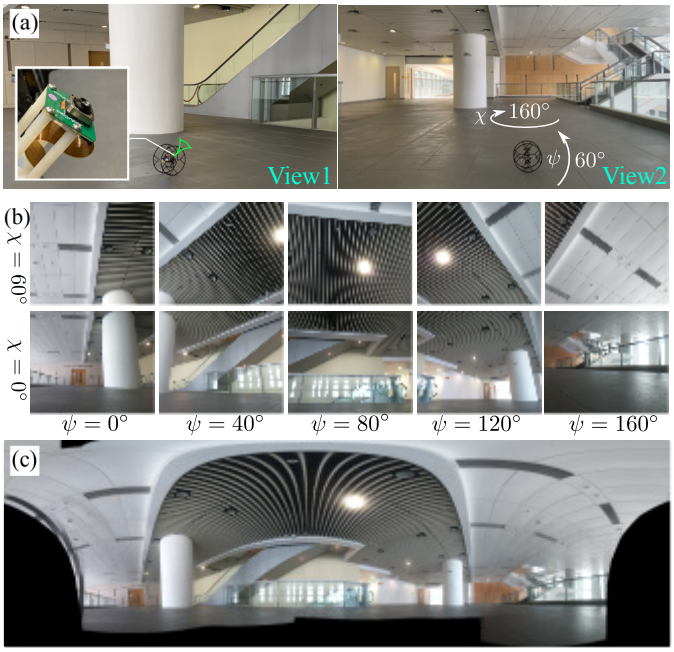

Fig. 7. (a) The robot with an onboard camera photographing the interior of a building. (b) Images taken by the onboard camera. The photos were from different camera panning ψ and tilting χ angles (10 out of 36 photos shown). (c) A panoramic image generated by stitching 36 images together.

in the RMSE of 28.8° over the 20-s period seen in Fig. 5e. Despite the non-negligible response time, the steady angular errors after each turn were only $\approx 5°$.

2) Pentagram Terrestrial Trajectory: Next, we show that a relatively sophisticated trajectory can be realized using the onboard IMU feedback by sequentially controlling the robot's rolling rate and turns. As a demonstration, we chose a pentagram-shaped path consisting of five 1.5-m straight-line segments and 144° turns. In this test, the commands of the rolling rates and turning directions were remotely transmitted to the robot by a human operator. Similar to the previous tests, the robot came to a complete stop prior to making a turn. The resultant trajectory, compared to the reference is presented in Fig. 5f. The robot completed the 7.5-m trajectory in 48 s.

3) Panoramic photography via precise control: We take advantage of the precise control in the terrestrial mode for the robot to take photos at various angles to construct one large panoramic image. A lightweight onboard camera (ArduCam 64MP with 84° FoV) was installed on the robot such that the optical axis points radially outwards from the center of the rolling frame, such that it is not always frontal (Fig. 7a). The robot took 36 photos of the surrounding, covering nine turning (camera panning) angular χ_d setpoints (20° apart) and four rolling (camera tilting) ψ_d angular setpoints (20° apart), by briefly staying stationary at each configuration to trigger the camera for non-blurry images (10 out of 36 images shown in Fig. 7b). As presented in Fig. 7c, after stitching by open-source software [32], a clear panoramic photo is generated.

Overall, these results show that the relatively simple methods for controlled rolling and turning are highly effective, attributable to the reconfigurable design of the airframe.

E. Power Consumption and Cost of Transport

For comparison, we determined the baseline power of the electronics without actuation for 10 minutes. The average power in the resting state was found to be 1.5 W.

1) Power consumption: To measure the power of the robot when rolling, the robot was set to travel back and forth along a 10-m line on three ground surfaces (vinyl flooring, brick tiles, and artificial turf). This was accomplished by switching the yaw rate setpoint between positive and negative values. This means the tests include periods of acceleration and deceleration. Three speeds were trialed: 0.5, 1.0, and 1.5 ms^{-1} on each surface. For each speed, the test lasted over four minutes. The averaged powers are plotted in Fig. 5g, monotonically increasing with the rolling speed.

A similar test was repeated with the robot flying. Since the robot expended considerably more energy in flight, we only flew the robot for one minute for each speed. At these speeds, the differences in the average power consumption are insignificant as seen in Fig. 5g. This is because the energy required to stay aloft is much higher than the power spent to overcome the aerodynamic drag at low flight speeds. Flying consumes $\approx 10-20$ times more energy than rolling.

2) Cost of transport: Taking into account the speeds, the dimensionless COT is calculated and shown in Fig. 5g. That is, rolling is up to ≈ 15 times as efficient as flying at these low speeds. The ratio of up to 15 in this work is higher than 3 demonstrated by a crawling-flying mini quadrotor [17] or ≈ 10 previously achieved by rolling quadrotors in [21], [26], likely due to the distinct propulsion mechanism for rolling of the proposed robot as manifested in Section II-A. When the terrain allows, terrestrial locomotion becomes a highly

appealing strategy for the robot to travel significantly further.

V. Conclusion

In this work, we have proposed a rotorcraft capable of controlled rolling and turning with a low cost of transport when traveling at low speeds. Unlike the existing design, the bimodal locomotion herein is enabled by a passively deformable airframe and a rolling cage. The use of revolute joints permits the thrust vectors to be re-oriented according to the control demands. In this form, the robot (i) rolls more efficiently; (ii) is able to directly accelerate/decelerate and control the turning and rolling motions, and (iii) takes a narrower profile while rolling. The performance of the robot in the aerial and terrestrial phases, as well as the transitions, was verified by a series of experiments. An example use of precise control in the terrestrial mode for a visual surveying task was presented. Furthermore, the power consumption of rolling was up to 15 times as low as that of flying. The degree of power saving compares favorably to previous hybrid quadrotors.

Although the Quadrolltor can proficiently control its rolling and turning using only its onboard IMU, on top of the flight ability. The reliance on a remote operator means the current development is still one step from accomplishing truly autonomous real-world operations such as reconnaissance. In the future, the integration of localization and mapping can be pursued to supplement the robot with the ability to navigate without human assistance in both operational modes.

References

[1] S. Tan, S. Zhong, and P. Chirarattananon, "A one-step visual-inertial ego-motion estimation using photometric feedback," *IEEE/ASME Transactions on Mechatronics*, vol. 27, no. 1, pp. 12–23, 2022.

[2] C. Campos, R. Elvira, J. J. G. Rodríguez, J. M. Montiel, and J. D. Tardós, "Orb-slam3: An accurate open-source library for visual, visual–inertial, and multimap slam," *IEEE Transactions on Robotics*, vol. 37, no. 6, pp. 1874–1890, 2021.

[3] X. Zhou, X. Wen, Z. Wang, Y. Gao, H. Li, Q. Wang, T. Yang, H. Lu, Y. Cao, C. Xu *et al.*, "Swarm of micro flying robots in the wild," *Science Robotics*, vol. 7, no. 66, p. eabm5954, 2022.

[4] K. Shah, G. Ballard, A. Schmidt, and M. Schwager, "Multidrone aerial surveys of penguin colonies in antarctica," *Science Robotics*, vol. 5, no. 47, p. eabc3000, 2020.

[5] W. Tabib, K. Goel, J. Yao, C. Boirum, and N. Michael, "Autonomous cave surveying with an aerial robot," *IEEE Transactions on Robotics*, vol. 38, no. 2, pp. 1016–1032, 2022.

[6] H. Hua, Y. Fang, X. Zhang, and C. Qian, "A new nonlinear control strategy embedded with reinforcement learning for a multirotor transporting a suspended payload," *IEEE/ASME Transactions on Mechatronics*, 2021.

[7] L. Bauersfeld and D. Scaramuzza, "Range, endurance, and optimal speed estimates for multicopters," *IEEE Robotics and Automation Letters*, vol. 7, no. 2, pp. 2953–2960, 2022.

[8] K. Karydis and V. Kumar, "Energetics in robotic flight at small scales," *Interface focus*, vol. 7, no. 1, p. 20160088, 2017.

[9] S. Bai, Q. He, and P. Chirarattananon, "A bioinspired revolving-wing drone with passive attitude stability and efficient hovering flight," *Science Robotics*, vol. 7, no. 66, p. eabg5913, 2022.

[10] M. A. Graule, P. Chirarattananon, S. B. Fuller, N. T. Jafferis, K. Y. Ma, M. Spenko, R. Kornbluh, and R. J. Wood, "Perching and takeoff of a robotic insect on overhangs using switchable electrostatic adhesion," *Science*, vol. 352, no. 6288, pp. 978–982, 2016.

[11] Y. H. Hsiao and P. Chirarattananon, "Ceiling effects for hybrid aerial–surface locomotion of small rotorcraft," *IEEE/ASME Transactions on Mechatronics*, vol. 24, no. 5, pp. 2316–2327, 2019.

[12] S. Park, D. S. Drew, S. Follmer, and J. Rivas-Davila, "Lightweight high voltage generator for untethered electroadhesive perching of micro air vehicles," *IEEE Robotics and Automation Letters*, vol. 5, no. 3, pp. 4485–4492, 2020.

[13] H.-N. Nguyen, R. Siddall, B. Stephens, A. Navarro-Rubio, and M. Kovač, "A passively adaptive microspine grapple for robust, controllable perching," in *2019 2nd IEEE International Conference on Soft Robotics (RoboSoft)*. IEEE, 2019, pp. 80–87.

[14] S. Kirchgeorg and S. Mintchev, "Hedgehog: Drone perching on tree branches with high-friction origami spines," *IEEE Robotics and Automation Letters*, vol. 7, no. 1, pp. 602–609, 2021.

[15] C. J. Pratt and K. K. Leang, "Dynamic underactuated flying-walking (duck) robot," in *2016 IEEE International Conference on Robotics and Automation (ICRA)*. IEEE, 2016, pp. 3267–3274.

[16] P. Ratsamee, P. Kriengkomol, T. Arai, K. Kamiyama, Y. Mae, K. Kiyokawa, T. Mashita, Y. Uranishi, and H. Takemura, "A hybrid flying and walking robot for steel bridge inspection," in *2016 IEEE International Symposium on Safety, Security, and Rescue Robotics (SSRR)*. IEEE, 2016, pp. 62–67.

[17] Y. Mulgaonkar, B. Araki, J.-s. Koh, L. Guerrero-Bonilla, D. M. Aukes, A. Makineni, M. T. Tolley, D. Rus, R. J. Wood, and V. Kumar, "The flying monkey: A mesoscale robot that can run, fly, and grasp," in *2016 IEEE international conference on robotics and automation (ICRA)*. IEEE, 2016, pp. 4672–4679.

[18] K. Kim, P. Spieler, E.-S. Lupu, A. Ramezani, and S.-J. Chung, "A bipedal walking robot that can fly, slackline, and skateboard," *Science Robotics*, vol. 6, no. 59, p. eabf8136, 2021.

[19] A. Kossett, J. Purvey, and N. Papanikolopoulos, "More than meets the eye: A hybrid-locomotion robot with rotary flight and wheel modes," in *2009 IEEE/RSJ International Conference on Intelligent Robots and Systems*, 2009, pp. 5653–5658.

[20] P. SA, *Parrot Minidrones Rolling Spider User Guide*, Parrot FA.

[21] A. Kalantari and M. Spenko, "Modeling and performance assessment of the hytaq, a hybrid terrestrial/aerial quadrotor," *IEEE Transactions on Robotics*, vol. 30, no. 5, pp. 1278–1285, 2014.

[22] R. Zhang, Y. Wu, L. Zhang, C. Xu, and F. Gao, "Autonomous and adaptive navigation for terrestrial-aerial bimodal vehicles," *IEEE Robotics and Automation Letters*, vol. 7, no. 2, pp. 3008–3015, 2022.

[23] K. Kawasaki, M. Zhao, K. Okada, and M. Inaba, "Muwa: Multi-field universal wheel for air-land vehicle with quad variable-pitch propellers," in *2013 IEEE/RSJ International Conference on Intelligent Robots and Systems*. IEEE, 2013, pp. 1880–1885.

[24] H. Jia, S. Bai, R. Ding, J. Shu, Y. Deng, B. L. Khoo, and P. Chirarattananon, "A quadrotor with a passively reconfigurable airframe for hybrid terrestrial locomotion," *IEEE/ASME Transactions on Mechatronics*, vol. 27, no. 6, pp. 4741–4751, 2022.

[25] E. Gefen and D. Zarrouk, "Flying star2, a hybrid flying driving robot with a clutch mechanism and energy optimization algorithm," *IEEE Access*, vol. 10, pp. 115 491–115 502, 2022.

[26] S. Atay, T. Jenkins, G. Buckner, and M. Bryant, "Energetic analysis and optimization of a bi-modal rolling-flying vehicle," *International Journal of Intelligent Robotics and Applications*, vol. 4, no. 1, pp. 3–20, 2020.

[27] S. Bai, R. Ding, and P. Chirarattananon, "A micro aircraft with passive variable-sweep wings," *IEEE Robotics and Automation Letters*, vol. 7, no. 2, pp. 4016–4023, 2022.

[28] N. Bucki, J. Tang, and M. W. Mueller, "design and control of a midair-reconfigurable quadcopter using unactuated hinges," *IEEE Transactions on Robotics*, vol. 39, no. 1, pp. 539–557, 2023.

[29] K. Patnaik and S. Mishra and S. M. R. Sorkhabadi and W. Zhang, "Design and Control of SQUEEZE: A Spring-augmented QUadrotor for intEractions with the Environment to squeeZE-and-fly," in *2020 IEEE/RSJ International Conference on Intelligent Robots and Systems (IROS)*. IEEE, 2020, pp. 1364–1370.

[30] L. Li and S. Wang and Y. Zhang and S. Song and C. Wang and S. Tan and W. Zhao and G. Wang and W. Sun and F. Yang and others, "Aerial-aquatic robots capable of crossing the air-water boundary and hitchhiking on surfaces," *Science Robotics*, vol. 7, no. 66, p. eabm6695, 2022.

[31] A. Fabris and E. Aucone and S. Mintchev, "Crash 2 Squash: An Autonomous Drone for the Traversal of Narrow Passageways," *Advanced Intelligent Systems*, vol. 4, no. 11, p. 2200113, 2022.

[32] M. Brown and D. G. Lowe, "Automatic panoramic image stitching using invariant features," *International journal of computer vision*, vol. 74, pp. 59–73, 2007.

IEEE Robotics and Automation Letters (RA-L) paper, presented at ICRA 2024, Yokohama, Japan. Cite as RA-L paper.